The effect of cell-to-cell variations and thermal gradients on the performance and degradation of lithium-ion battery packs

Xinhua Liu[1], Weilong Ai[1,2], Max Naylor Marlow[1], Yatish Patel[2,3], and Billy Wu[1,2*]
[1]Dyson School of Design Engineering, Imperial College London, UK
[2]The Faraday Institution, Quad One, Harwell Science and Innovation Campus, Didcot, UK
[3]Department of Mechanical Engineering, Imperial College London, UK
*e-mail of corresponding author: billy.wu@imperial.ac.uk

Key words: Lithium-ion battery, Packs, Thermal gradients, Degradation

Abstract

The performance of lithium-ion battery packs are often extrapolated from single cell performance however uneven currents in parallel strings due to cell-to-cell variations, thermal gradients and/or cell interconnects can reduce the overall performance of a large scale lithium-ion battery pack. In this work, we investigate the performance implications caused by these factors by simulating six parallel connected batteries based on a thermally coupled single particle model with the solid electrolyte interphase growth degradation mechanism modelled. Experimentally validated simulations show that cells closest to the load points of a pack experience higher currents than cells further away due to uneven overpotentials caused by the interconnects. When a cell with a four times greater internal impedance was placed in the location with the higher currents this actually helped to equalise the cell-to-cell current distribution, however if this was placed at a location furthest from the load point this would cause a ~6% reduction in accessible energy at 1.5 C. The influence of thermal gradients can further affect this current heterogeneity leading to accelerated aging. Simulations show that in all cases, cells degrade at different rates in a pack due to the uneven currents, with this being amplified by thermal gradients. In the presented work a 5.2% increase in degradation rate, from -7.71 mWh/cycle (isothermal) to -8.11 mWh/cycle (non-isothermal) can be observed. Therefore, the insights from this paper highlight the highly coupled nature of battery pack performance and can inform designs for higher performance and longer lasting battery packs.

Nomenclature

ϵ	Volume fraction of the solid phase in the electrode
η	Electrochemical overpotential (V)
η_s	Overpotential of the side reaction
κ_p	Conductivity of the SEI (S/m)
Φ	Electrode potential (V)
Ψ	Property of interest
Ψ_{ref}	Property value defined at the reference temperature T_{ref} (K)
ρ	Density of the cell (kg/m^3)

ρ_P Density of the SEI (kg/m^3)

A_s Convective surface area of the battery (m^2)

C_p Specific heat capacity (J/kg/K)

D Diffusion coefficient (m^2/s)

E_{act}^{Ψ} Thermal activation energy corresponding to Ψ (J/mol)

F Faraday's constant

I Whole cell current density externally provided (A/m^2)

I^+ Positive electrode current density (A/m^2)

I^- Negative electrode current density (A/m^2)

I_{app} Applied current density (A/m^2)

I_s Reaction current density of the side reactions (A/m^2)

L Thickness of the electrode (m)

M_P Molecular weight of the SEI (mol/kg)

R Universal gas constant (J/mol/K)

R_{film} Solid electrolyte interphase (SEI) layer resistance (Ω.m^2)

R_s Series resistance (Ω)

R_s^+ Radii of the cathode (m)

R_s^- Radii of the anode (m)

R_{SEI} Initial SEI layer resistance (Ω.m^2)

T Temperature (K)

T_∞ Ambient temperature (K)

U Thermodynamic electrode potential (V)

a_s Specific surface area of the electrode (m^2/m^3)

c Concentration of lithium in the solid phase (mol/m^3)

h Convective heat transfer coefficient (W/m^2)

i_{0s} Reaction current density of the side reaction

k_{eff} Effective conductivity of the electrolyte (S/m)

q_e Electronic ohmic heat from material electronic resistances (W)

q_j Heat from the reaction current (W)

r Radius of the particle (m)

t Time (s)

x_n Stoichiometry of the anode

Introduction

With the rapidly increasing uptake of electric vehicles and intermittent renewable technologies such as wind and solar, there is a strong need for energy storage technologies. Of the various storage technologies, lithium-ion batteries are currently the most commercially mature however there are still technical challenges to overcome [1–5]. When integrating kWh to MWh-scale battery systems, hundreds to thousands of cells are connected in series and parallel. For the effective operation of the battery pack, cell-to-cell consistency and thermal uniformity is extremely important [5–9], however, these effects are not often discussed in the literature and statistically significant results are seldom found.

Rumpf et al. [10] is one of the few exceptions and in their investigation of cell-to-cell variations they tested 1,100 fresh commercial lithium iron phosphate (LFP) cells. By using a combination of charge/discharge and electrochemical impedance spectroscopy tests, they showed that the relative variation in capacity and impedance is small; 0.28% and 0.72% respectively. However, these measurements were made for fresh cells and the evolution of these metrics over time has been shown to deviate significantly. Baumhöfer et al. [11], for instance, performed an analysis with 48 Sanyo/Panasonic nickel manganese cobalt oxide (NMC) cylindrical cells and showed that the capacity variation at the end of life significantly deviated from that of the initial life. Harris et al. [12] analysed the failure statistics of 24 commercial lithium cobalt oxide pouch cells with almost 600 charge/discharge cycles and found significant deviation in the failure point of cells from the same batch which broadly fit a normal or a 2-parameter Weibull probability density function though more data is needed to increase the confidence. Here the capacities dropped to between 45% and 85% although cells were tested at a high rate of 10 C to accelerate the degradation processes, which likely increased the variation in performance.

At the pack level, variations in cell performance or interconnect resistances can lead to heterogeneous current distributions in parallel strings [13–17] and subsequent acceleration of the degradation compared to the equivalent single cell performance [18–21]. The root cause of this heterogeneous current distribution and hence accelerated degradation can be attributed to effects such as uneven thermal conditions, columbic efficiency variations and self-discharge rates, amongst others [21–24]. Offer et al. [25] developed a lithium-ion battery pack consisting of 508 4.8 Ah lithium polymer batteries and showed that intercell connectors can have significant pack level performance implications due to the interconnection overpotential inducing higher currents in some cells of the same parallel string. Carter et al. [26] used x-ray computed tomography to show that parallel connected LFP cells cycled at 10 C exhibited accelerated degradation in the pack configuration and that the root cause of this was localised over-discharge leading to copper current collector dissolution and thus an increase in series resistance.

To quantify the impact of parallel connections authors have generally used either an equivalent circuit model [15,16,20,27–29] or physics based modelling approaches [13,21,24,30]. Wu et al. [13] for instance, developed a battery pack model using a set of pseudo-2D electrochemical-thermally coupled lithium-ion battery models in addition to interconnects and quantified the effect of these additional cell-to-cell resistances. They showed that these interconnects can lead to significant uneven heat generation and other effects such as charge redistribution between cells, which can arise due to the pack construction and thus highlights the importance of capturing the physical processes occurring in a pack. Merla et al. [31,32] further showed that introducing degraded cells in a parallel string of cells leads to significant and highly non-linear discharge profiles. Since the degradation of lithium-ion batteries is highly usage dependent [33,34] this will lead to further non-linear and heterogeneous degradation.

Yang et al. [35] used a thermal-electrochemical model to investigate the impact that temperature has on unbalanced discharging and aging of parallel connected lithium-ion batteries. They show that cells at higher temperature provide more current until approximately 75% of the depth of discharge which coincides with the voltage drop-off of the discharge profile. At this point the current distribution switches due to increases in cell impedance. They show that for parallel-connected battery packs, the rate of capacity loss increases linearly with temperature difference, and the rate accelerates with increasing operating temperature.

Further modelling from Bruen and Marco [36] showed that a 30% difference in cell impedance can result in a 60% difference in peak cell current. Gogoana et al. [30] showed that 2 parallel connected cells with a 20% difference in internal resistance can result in a 40% reduction in cycle life when compared to cells with matched internal resistances. This pack level non-uniform behaviour becomes even more critical as hybrid systems using different chemistries are investigated [37].

However, in nearly all pack level modelling work involving lithium-ion batteries, the authors have assumed that all cells have the same performance with limited works also considering the effect of thermal gradients. Yet, it is well known that there is a performance distribution between cells that exist due to small variations in the manufacturing in the cells which can lead to uneven heat generation. The result is that some cells have higher/lower capacities and impedances, with this distribution varying depending on many factors such as the manufacturing quality, age and other factors.

Thus, it becomes apparent that there is a need to understand how these cell-to-cell variations and practical thermal conditions affect the performance of lithium-ion battery packs and come up with design rules to mitigate the detrimental effect of performance variation. In this work, a thermally coupled single particle model (SPM) approach is taken to model the impact of cell-to-cell variations and thermal gradients on battery pack performance and lifetime to inform better pack designs. Key insights developed include the quantification of performance differences between single cells and parallel cells in packs which is important for automotive manufacturers to consider otherwise they risk overestimating performance and lifetime. Furthermore, the performance and lifetime implications of positioning cells with different resistances in these packs as well as different thermal gradients is presented which is critical when designing a pack. Coupled with pack level

diagnostics considerations, these novel insights are therefore of critical importance for pack manufacturers to consider and are not often discussed in the academic literature.

Single particle model

Modelling lithium-ion batteries is an essential part of effective system design. At a high level, there are a number of different types of models. Equivalent circuit models simulate the transient voltage response of batteries through the combined use of capacitors, resistance, voltage sources and other components [38,39]. The advantage of these models is that they run quickly, however they generally lack detailed physical insight which means effects such as degradation and coupled thermal effects are challenging to capture. Data driven models such as neural networks have the advantage that generic models can be developed without the need to understand the underlying physics, however large datasets are required to train the models and again, a deep physical understanding of the processes occurring is lacking [40,41]. Electrochemical models have the advantage that they capture physical processes such as charge transfer and diffusion of species however they often require the solution of coupled differential equations which results in a computationally expensive solution. Despite the computational requirements, electrochemical models are often seen as the modelling technique of choice for detailed analysis due to the retention of the physical processes. There are a number of different types of electrochemical modelling at the cell level which includes 3D [42], 2D, 1D [13,43–48] and 0D [49–53] forms.

For this work, a 0D or single particle model (SPM) approach was adopted from the work by Chaturvedi and Klein [52] and Ramadass et al. [53] due to the ability to capture physical processes such as diffusion whilst being computationally cheap enough to allow for multiple cells to be modelled simultaneously.

The potential of a lithium-ion battery is defined by the difference in the anode and cathode potentials, the current and the series resistance as defined by Equation 1. Here Φ represents the electrode potential (V), R_s the series resistance (Ω), I the current (A) and the superscripts + and –, the positive and negative electrodes respectively. The potential of the cathode and anode are described by Equations 2 and 3, where η is the electrochemical overpotential (V), U is the thermodynamic electrode potential, or Open Circuit Potential (OCP), which is defined by the state of lithiation, R_{film} is the solid electrolyte interphase (SEI) layer resistance ($\Omega.m^2$), a_s is the specific surface area of the electrode (m^2/m^3) and L the thickness of the electrode (m). The specific surface area of the anode and cathode are described by Equations 4 and 5 respectively, where ϵ is the volume fraction of the solid phase and R_s^- and R_s^+ are the radii of the anode and cathode respectively.

The anode has an extra term which describes the electrode potential due to the presence of the SEI layer, which is a cause of degradation in lithium-ion batteries. This surface film grows over the lifetime of the battery causing capacity fade and power fade as the film grows. In the SPM it is assumed that no lithium-ion diffusion gradients exist in the electrolyte and thus the electrolyte potential is zero ($\Phi_e = 0$).

$$V = \Phi^+ - \Phi^- - R_s I \quad (1)$$

$$\Phi^+ = \eta^+ + U^+ \quad (2)$$

$$\Phi^- = \eta^- + U^- + \frac{R_{film} I}{a_s^- L^-} \quad (3)$$

$$a_s^- = \frac{3\epsilon^-}{R_s^-} \quad (4)$$

$$a_s^+ = \frac{3\epsilon^+}{R_s^+} \quad (5)$$

The overpotential of an electrochemical device can be described by the Butler-Volmer equation. The SPM approximates this to Equations 6 and 7 [52]. Here R is the universal gas constant (J/mol/K), T is the temperature (K), k_{eff} is the effective conductivity of the electrolyte (S/m), c is the concentration of lithium in the solid phase (mol/m^3) and the subscripts e, s and max represent the electrolyte, solid phase and maximum solid phase lithium-ion/ lithium content. I is the whole cell current density (A/m^2) externally provided, I_{app} is the current density (A/m^2) which drives the main battery reactions and I_s is the reaction current density of the side reactions (A/m^2) which arise from the growth of the SEI layer.

$$\eta^- = \frac{2RT}{F} \sinh^{-1}\left(\frac{I_{app}}{2a_s^- L^- k_{eff}\sqrt{c_e c_s^- (c_{max}^- - c_s^-)}}\right) \quad (6)$$

$$\eta^+ = \frac{2RT}{F} \sinh^{-1}\left(\frac{I_{app}}{2a_s^+ L^+ k_{eff}\sqrt{c_e c_s^+ (c_{max}^+ - c_s^+)}}\right) \quad (7)$$

$$I = I_{app} + I_s \quad (8)$$

The thermodynamic electrode potentials are a function of the lithium content. Here the anode OCP is described by Equation 9 which is taken from Ramadass et al. [53]. Here x_n is the stoichiometry of the anode as described in Equation 10. The cathode OCP is defined based on fitting of experimental data described in later sections.

$$U^- = 0.7222 + 0.1387.x_n + 0.029.x_n^{0.5} - \frac{0.0172}{x_n} + \frac{0.0019}{x_n^{1.5}} + 0.2808e^{(0.9-15x_n)} - 0.7984e^{(0.4465x_n - 0.4108)} \quad (9)$$

$$x_n = \frac{c^-(r = R_s^-)}{c_{max}^-} \quad (10)$$

As apparent from Equations 9 and 10, the potential of an electrode is defined by the surface concentration of lithium in the solid phase. In the SPM, it is assumed that the solid-state lithium concentration can be described by a single spherical particle in each electrode and Ficken diffusion as described in Equation 11. Here t is the time (s), r the radius of the particle (m), D the diffusion coefficient (m^2/s). The boundary conditions for both the anode and cathode are described by Equation 12 and 13. Here no lithium flux exists at the centre of the particle and the flux at the surface is dictated by the reaction current. Here the subscripts + and – represent the positive and negative electrodes respectively, R is the radius of the particle and F is Faraday's constant.

$$\frac{\partial c}{\partial t} = \frac{1}{r^2}\frac{\partial}{\partial r}\left(Dr^2\frac{\partial c}{\partial r}\right) \quad (11)$$

$$\left.\frac{\partial c^-}{\partial r}\right|_{r=0} = 0, \quad \left.\frac{\partial c^-}{\partial r}\right|_{r=R_s^-} = -\frac{I_{app}}{D^- F a_s^- L^-} \quad (12)$$

$$\left.\frac{\partial c^+}{\partial r}\right|_{r=0} = 0, \quad \left.\frac{\partial c^+}{\partial r}\right|_{r=R_s^+} = \frac{I_{app}}{D^+ F a_s^+ L^+} \quad (13)$$

In this model, the only assumed degradation mode is the growth of the SEI layer on the anode. This causes capacity fade through the consumption of cyclable lithium during the growth of the passivating layer, but also causes power fade through an increase in the resistance of the film growth and is often cited as the dominate mode of capacity/power fade. The growth rate of the SEI was described by Butler-Volmer kinetics by using a Tafel approximation as shown in Equation 14.

$$J_s = -i_{0s} a_s^- exp^{-\frac{F}{2RT}\eta_s} \quad (14)$$

Here, i_{0s} is the reaction current density of the side reaction and η_s is the overpotential of the side reaction which can be defined by Equation 15.

$$\eta_s = \Phi_s - \Phi_e - U_s - \frac{J}{a_s^-} R_{film} \quad (15)$$

Finally, the growth rate of the SEI layer can be defined by Equation 16 where M_P is the molecular weight (mol/kg) of the SEI and ρ_P is the density of the SEI (kg/m^3).

$$\frac{\partial \delta_{film}}{\partial t} = -\frac{J_s M_P}{a^- \rho_P F} \quad (16)$$

Following the calculation of the growth rate, the film resistance can be calculated from Equation 17, where R_{SEI} is the initial SEI layer resistance (Ω.m^2) and κ_p is the conductivity of the SEI (S/m).

$$R_{film} = R_{SEI} + \frac{\delta_{film}}{\kappa_p} \quad (17)$$

The temperature of a lithium-ion battery plays a key role in the performance and lifetime of the cell with low temperatures potentially resulting in 2 orders of magnitude difference in the internal resistance [54] and elevated temperatures resulting in accelerated degradation. Heat generation in a cell can be attributed to 4 main influences: electronic ohmic heat from material electronic resistances (q_e), heat from the reaction current (q_j), diffusion heat from the motion of lithium/lithium-ions through the solid and electrolyte phase, and reversible entropic heat caused by phase changes in electrodes. In the majority of cases, the entropic heat is much smaller in magnitude than the other heat generation terms and can be neglected [43]. Also, since there are no lithium-ion electrolyte concentration gradients in the SPM, that heat term drops out and does not need to be considered. Furthermore, the heat

generated from the solid phase was found to be smaller than that of the series and reaction heats, thus was neglected [43]. Therefore, 2 heat generation terms arise as described by Equations 18 and 19.

$$q_e = I^2 R_s \quad (18)$$

$$q_j = I(\eta^- + \eta^+) \quad (19)$$

These source terms are then combined with a lumped thermal model as described by Equation 20 which assumes free convection is the only means of heat removal. Here ρ is the density (kg/m^3), C_p is the specific heat capacity (J/kg/K), h is the convective heat transfer coefficient (W/m^2), A_s is the convective surface area of the battery (m^2) and T_∞ is the ambient temperature (K).

$$\frac{\partial(\rho C_p T)}{\partial t} = q_e + q_j - hA_s(T - T_\infty) \quad (20)$$

The temperature of the battery will have an impact predominantly on the electrochemical reactions and the rate of diffusion, with both being faster has higher temperatures. This is described with an Arrhenius rate law equation as shown in Equation 21 where Ψ is the property of interest (e.g. the solid-state diffusion coefficient D, the effective electrolyte conductivity k_{eff} or the exchange current density i), Ψ_{ref} is the value of the variable defined at the reference temperature T_{ref} (K), and E_{act}^{Ψ} (J/mol) is the thermal activation energy corresponding to Ψ. Here T_{ref} is defined as 293.15 K with the simulated temperature taken as the average temperature of the cell, as a lumped thermal model (0D) was used.

$$\Psi = \Psi_{ref} exp\left[\frac{E_{act}^{\Psi}}{R}\left(\frac{1}{T_{ref}} - \frac{1}{T}\right)\right] \quad (21)$$

The simulated discharge curves from the SPM are shown in Fig. 1(a) and the resulting temperature increase is shown in Fig. 1(b). As C-rate increases, the observed overpotential also increases resulting in a lower output voltage and thus reaching the 2.7 V cut-off earlier; reducing the accessible capacity. The heat generation also increases with C-rate due to the higher applied currents.

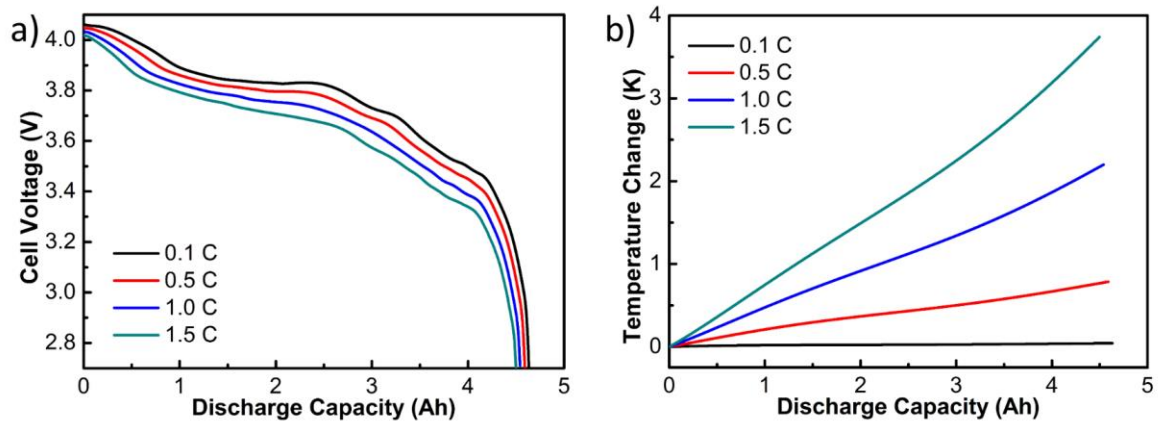

Fig. 1. (a) Simulated discharge curve V-Ah and (b) their temperature increase for different C-rates for a single cell (0.1C, 0.5C, 1C and 1.5 C).

Lithium-ion battery pack simulation and validation

In order to probe the pack level performance implication of cell-to-cell variations and thermal gradients, the SPM equations were implemented into the MATLAB programming environment, where the parameters for battery cells are the same as reported in Patsios et al. [49], with several cells assembled into a pack within the Simulink SimPowerSystems toolbox. Between each cell finite interconnect resistances were added to represent bus bars and contact resistances. A schematic of a 6P1S configuration is shown in Fig. 2.

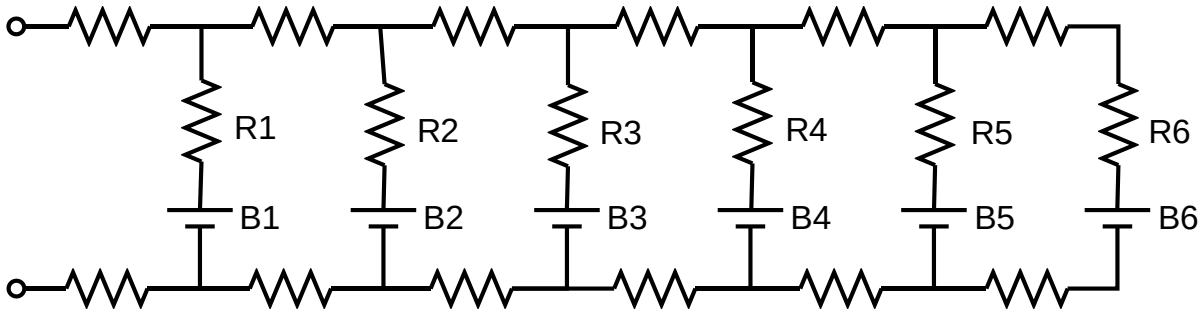

Fig. 2. Schematic layer out of the modelled 6P1S battery pack configuration with interconnect resistances.

In the modelled lithium-ion batteries, which are based on cells from Kokam, the operating voltage window is 4.2-2.7 V. In the majority of lithium-ion battery models focusing on automotive and grid applications, the performance of the pack is often inferred from single cell performance, however they neglect to account for the interconnection resistances which can cause a significant deviation from the single cell performance. This is highlighted in Fig. 3 where it can be seen that at low C-rates (0.1 C) the performance of the cell and pack are reasonably consistent, however when C-rates are increased to 1.5 C the variation in cell voltage is much more substantial.

This observed variation between the single cell and pack performance can be attributed to the interconnect resistances which can cause uneven current distributions as highlighted in

Fig. 4 for a discharge rate of 0.25 C and 1 C. Here both the simulated and experimental results show good agreement and highlights the fact that upon initial application of the load, the cell closest to the load point experiences the highest current due to lower interconnect overpotentials [13]. A decrease in the load current is then observed in cells further from the load point, however as the pack discharges the load rebalances due to differences in state-of-charge (SOC) and subsequent impedance changes. As the current is increased it can be seen that there is an increase in the current heterogeneity. Fig. S1 (supplementary information) shows uneven current distributions at discharge rates of 0.5 C and 0.75 C which demonstrate the same trends.

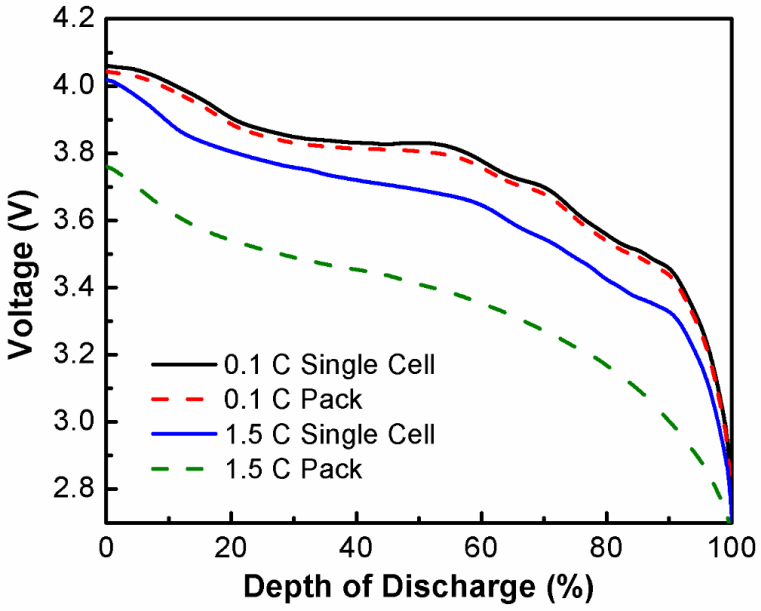

Fig. 3. Simulated voltage against normalised capacity at 0.1 C and 1.5 C in the single cell and 6P1S battery pack configuration.

Pack experimental set-up

In order to validate the model, experiments were carried out using 5 Ah Kokam SLPB11543140H5 lithium-polymer cells. The cells used contain a graphite negative electrode and composite NMC-LCO positive electrode, and were arranged in a 6P1S parallel string configuration. The experimental setup was designed such that it reproduced the model and therefore, (10±1%) mΩ resistors were placed in between each parallel branch with (1±5%) mΩ interconnect resistors measuring the current into each cell. The value of the resistor was selected based on reported values in the literature [55,56]. a 50 A BaSyTec XCTS Battery Test System, the pack was charged to 4.2 V prior to each test with a CC-CV hold with a cutoff at C/100. The pack was then discharged to 3.0 V at rates of 0.25 C, 0.5 C, 0.75 C and 1 C. To validate results with varied cell resistances, additional (10 ±1%) mΩ resistors were added to the parallel branches where required. The resistors were soldered onto laser cut 1 mm aluminium sheets which acted as the interconnection points, with the cell tabs firmly compressed against the interconnects. The experimental set-up of the 6P1S parallel string configuration is shown in Fig. S2. The current to each cell was calculated using the measured voltage across the current sense resistors using a 16 bit analogue to

digital converter (ADS1115). All tests were conducted at room temperature. Current sense resistors were calibrated prior to testing using a BioLogic HPC-1005 potentiostat with a sampling rate of 1 Hz.

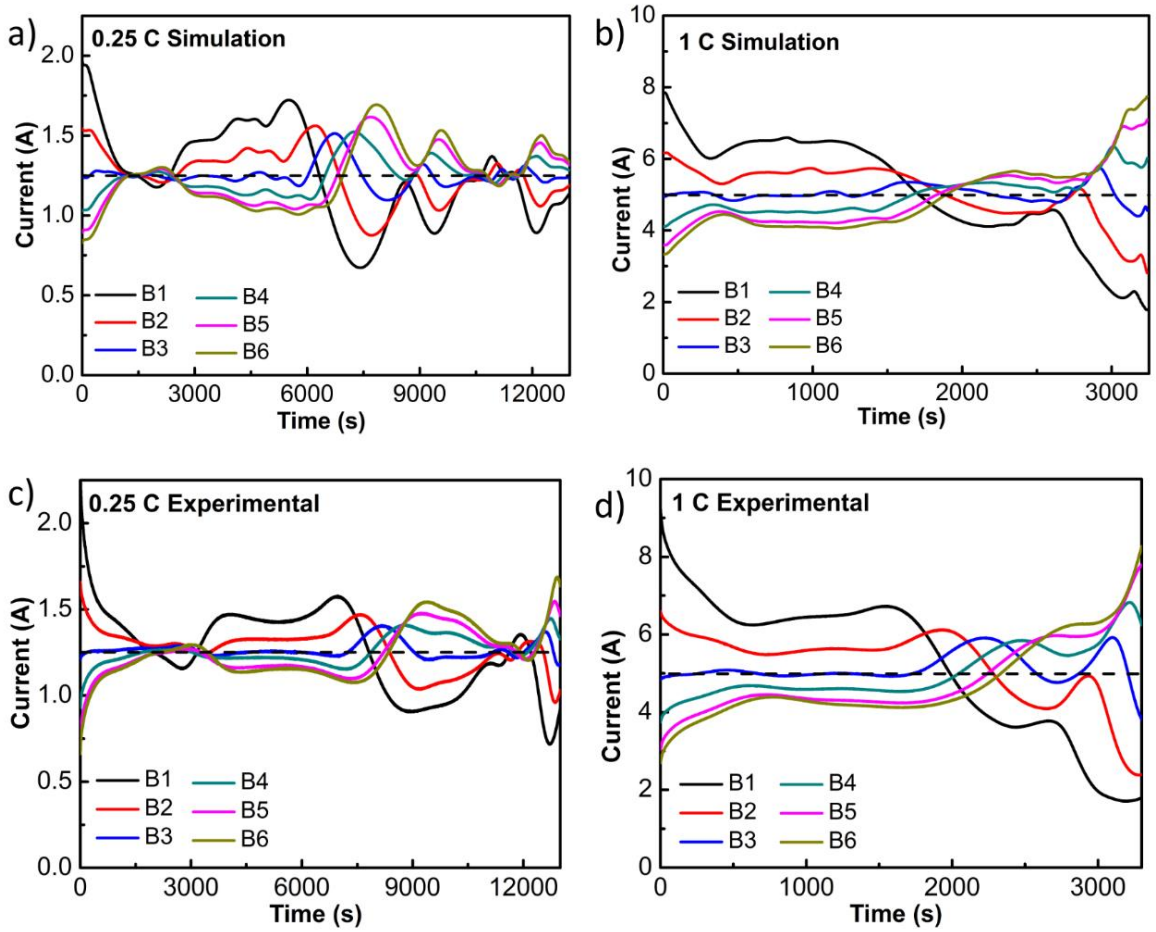

Fig. 4. Current distribution plots for a 6P1S battery pack with all the same cells. Simulated results at 0.25 C (a) and 1 C (b) as well as experimental results at 0.25 C (c) and 1 C (d). Dashed lines represent the nominal cell discharge current with a given C-rate applied to the pack.

The complex nature of the uneven current distribution is further highlighted and quantified in Fig. 5 where the standard deviations between the cell currents are presented. In an ideal battery pack, current is split evenly between cells as uneven currents lead to localised heating, a reduction in the accessible capacity and thus accelerated degradation. Again, the simulated and experimental results are in good agreement. Under all C-rates there is an initially high variation in the parallel cell currents, however as the SOCs vary, the non-linear change in the impedance results in complex current distributions. In cases where the discharge currents are above 0.25 C there is an increase is the standard deviation at the end of the SOC which indicates increased localised heating of the cells furthest from the load point. Thus, suitable temperature monitoring is essential to prevent thermal runaway. The average standard deviation of currents over the discharge cycle at different C-rates also highlights that this deviation increases as the C-rate is increased. Here good agreement between the model and the experiments are observed at C-rates of 0.5 C and below, however there is an underestimation above this point. This is due to the simplifications

applied in the SPM model used which do not capture lithium-ion concentration gradients in the electrolyte well, thus underestimating the cell overpotential.

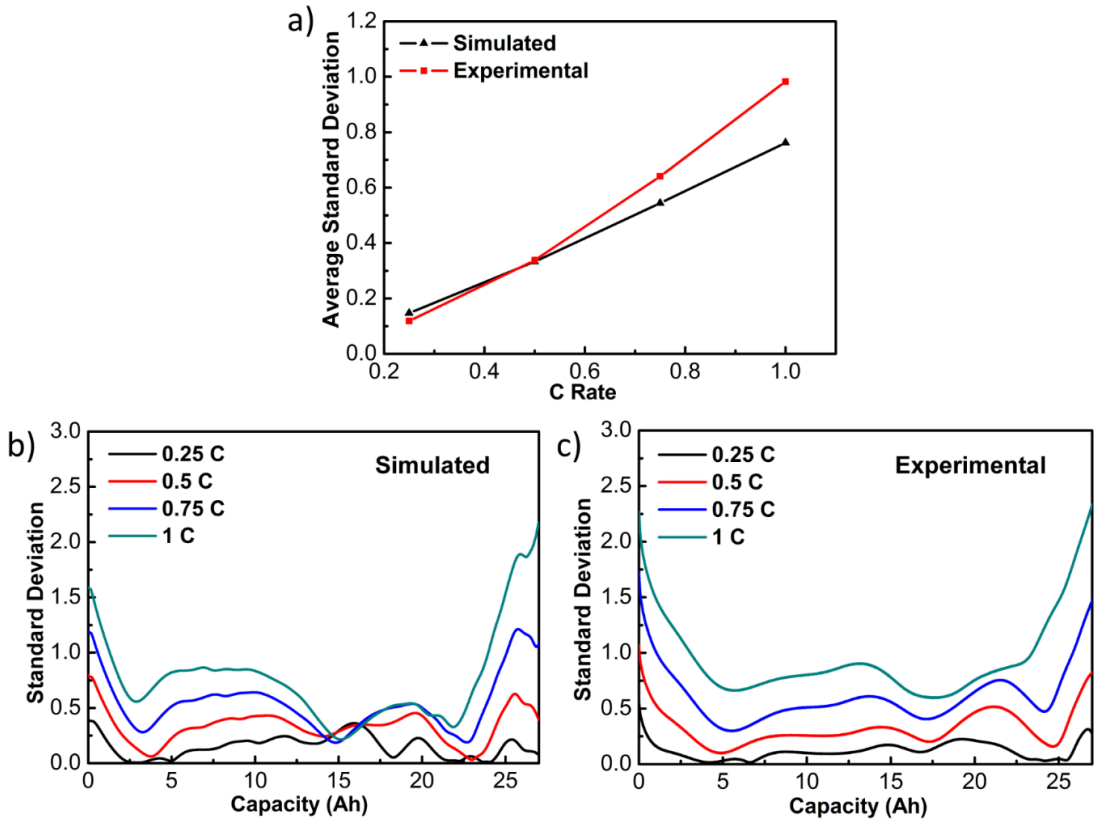

Fig. 5. (a) The average standard deviation at different C-rates obtained from simulation and experiment of a 6P1S battery pack with all cells with the same parameters. Standard deviation of cell currents during discharging at different C-rates of a 6P1S battery pack with all cells with the same parameters from simulation (b) and experiment (c).

This modelling framework can also be used to probe the effect of cell-to-cell variation in battery packs, which is seldom reported. Fig. 6 highlights the different performance observed when a cell with a higher impedance is combined with cells of a lower impedance. Fig. 6(a) shows the current distribution for a 6P1S battery pack with cells with the same condition for all six cells (their positions are named as B1–B6 inline with Fig. 2). Here it can be seen that the cell closest to the load point (B1) experiences an initial current 188% larger than the cell furthest from the load point (B6) at 0.5 C. After approximately 50% depth-of-discharge, this trend is switched due to differences in the SOC. If a battery with a 400% increase in series resistance was then added to the parallel string this would change the current distribution however the positioning of this cell has implications on pack performance. Fig. 6(b) shows that if the cell with a higher resistance is placed in position (B1) then this actually has beneficial implications on the performance as the higher resistance helps to balance to unequal load. This is in contrast to Fig. 6(c), where the cell is placed at location B6 which exacerbates the uneven current distribution. The results shown in Fig. S3 shows the same argument with a 200% increase in series resistance with the experimental data showing good agreement with the simulations.

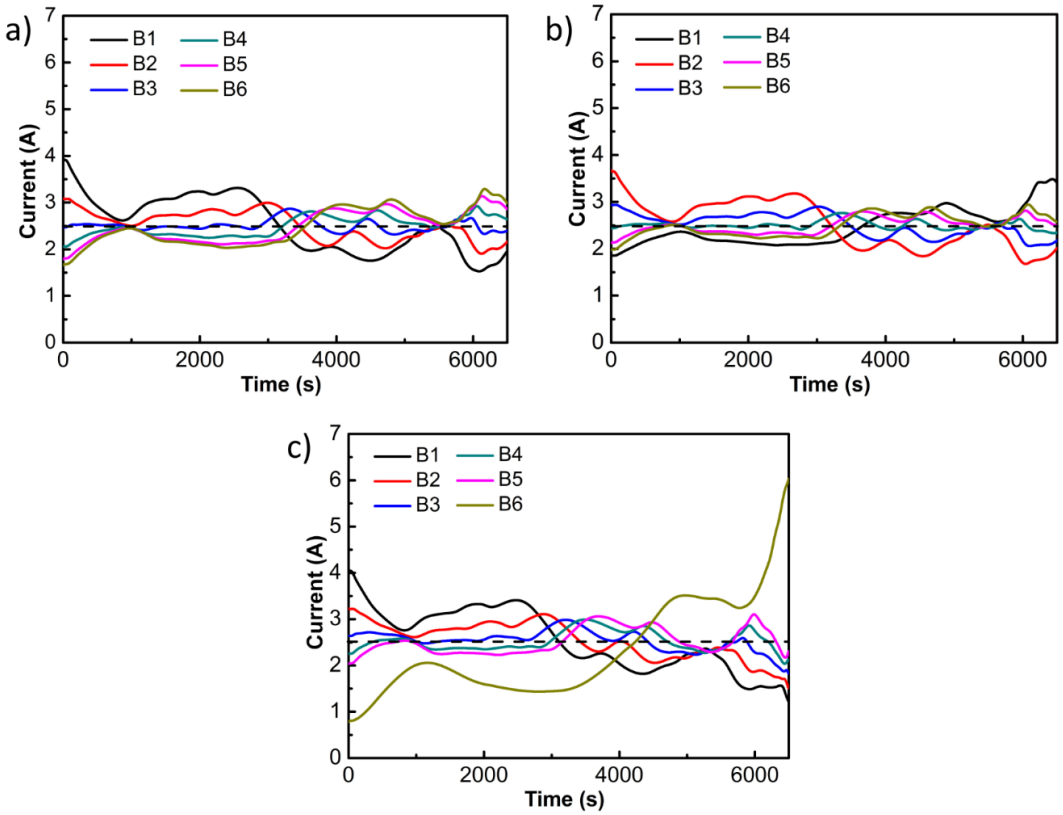

Fig. 6. Simulated current distribution plots for a 6P1S battery pack with (a) all cells with the same parameters; (b) a cell with 400% higher internal resistance near the loading point (B1); (c) a cell with 400% higher internal resistance further from the loading point (B6). Dashed lines represent the nominal cell discharge current with a given C-rate applied to the pack.

Furthermore, Fig. 7(a) shows how the standard deviation of the cell currents varies over a discharge when the cell is placed in different locations. Fig. 7(b) then shows how the average of this standard deviation varies as a function of the C-rate and the cell position. Both Fig. 7(a) and Fig. 7(b) deliver the same information that the current distribution is more homogenous when a cell with a higher resistance is placed in the location of highest load. This further highlights that cell positioning is highly important and that this becomes even more important at high C-rates as the higher currents can lead to larger average standard deviation.

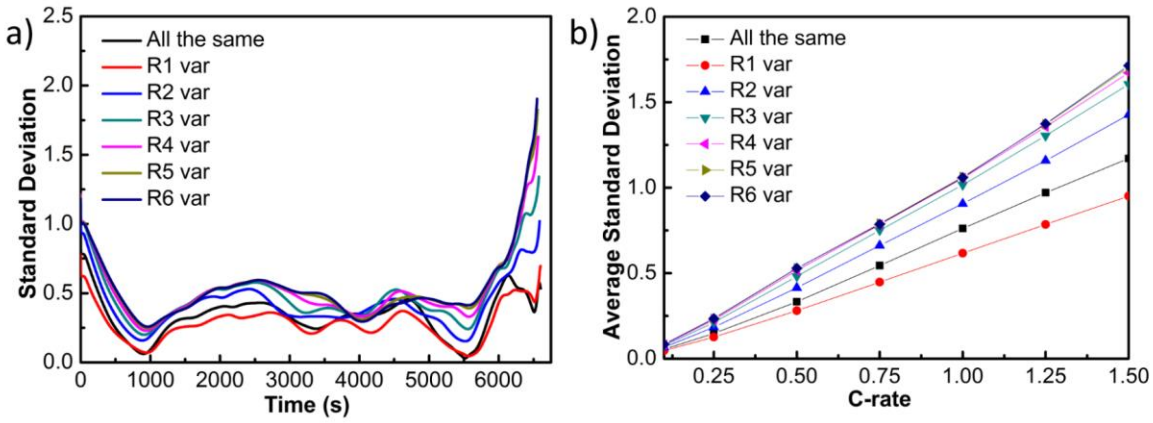

Fig. 7. Simulated standard deviation of cell currents during a discharge of a 6P1S battery pack where the poor cell is located in different positions and the average standard deviation at different C-rates

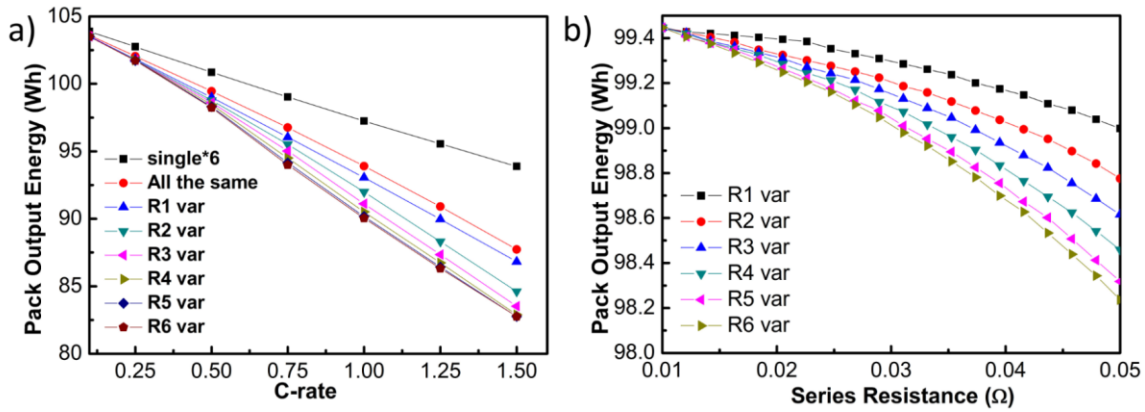

Fig. 8. a) Simulated pack output energy as a function of C-rate and cell positioning for a 6P1S battery pack. b) Simulated pack output energy as a function of resistance variations and cell positioning for a 6P1S battery pack at 0.5 C. Series resistances vary (20 points) from 0.01 Ω to 0.05 Ω.

Fig. 8 then shows how the pack output energy varies as a function of the cell positioning and also the C-rate. At low C-rates, the benefits of this grouping are negligible, however at higher C-rates (1.5 C) this can make up to 6% difference (Fig. 8(a)). Additionally, different values of resistances lead to different output energy for the battery pack even at the same C-rate. As shown in Fig. 8(b), both the position and the resistance variation values can lead to changes in output energy (0.5 C). For the same location, higher resistance leads to lower battery pack output energy, however for the same resistance value, suitable cell placement can mitigate the impact of the resistance variation.

Quantification of the impact of cell-to-cell variations can be extended to Fig. 9(a) which shows the Ragone plot of the 6P1S battery pack as a function of cell positioning. Here the calculation is based on the commercial Kokam cells with a 5 Ah capacity and 132 g mass for a single cell. The battery pack with all the same cells achieve highest energy and power densities compared with the battery pack with a cell of higher resistance. However, the placement of the cell can affect the energy and power density, with the placement of higher impedance cells nearer the load points beneficial.

Being able to diagnose these effects is also important. Fig. 9(b) presents the incremental capacity analysis (ICA) of the battery pack with the different cell placements and it can be clearly seen that due to the heterogeneous current distribution, the ICA profiles are modified. In both cases of introducing the higher impedance cell, there is a shift in the main peak at 3.45V to lower potentials due to the increased resistance of the overall pack. In the case where the cell is placed in position B6, the area of the curve is also reduced, indicating a reduced accessible capacity which is also highlighted in the Ragone plot.

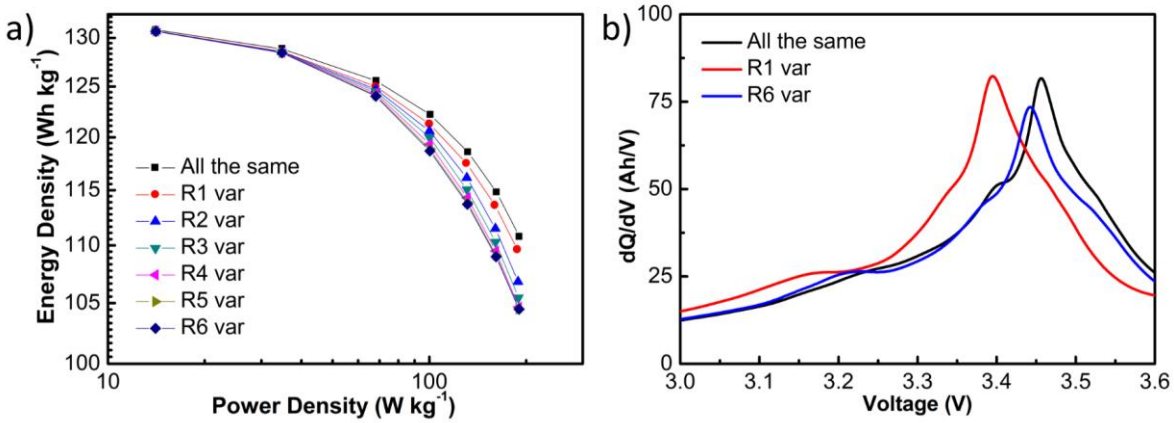

Fig. 9. a) Simulated energy density vs power density for different cell positioning for a 6P1S battery pack. b) Simulated incremental capacity analysis profiles for different pack configurations under 1.5 C constant current discharge.

The effect of thermal gradients in battery packs

The influence of thermal gradients on battery packs has also been studied in this work. Here, different thermal gradients are considered, and for easy illustration the following notations are used: “20-45” corresponds to 5 °C increments from 20 °C to 45 °C for cells B1 to B6 respectively; “45-20” corresponds to 5 °C reductions from 45 °C to 20 °C for cells B1 to B6 respectively; “32.5-all” corresponds to isothermal conditions (32.5 °C) being set for all cells; similarly “20-all” and “45-all” correspond to isothermal conditions of 20 °C and 45 °C respectively.

The Ragone plot of the battery packs under different thermal gradients is shown in Fig. 10(a). The battery pack with an high isothermal temperature (45 °C) provides the highest energy/power densities, while the performance of the pack with all cells at 20 °C are the lowest. This should be expected due to the reduction in the cell impedance with increasing temperature and faster solid-state lithium diffusion in the electrodes. Although cells with higher temperatures demonstrate improved energy densities, temperature gradients can affect the performance of battery packs in complex ways due to the non-linear thermo-electrochemical properties of cells. The “20-45” pack, with the lower temperature cells closer to the load point, achieves a higher energy/power density than the counterpart (“45-20” pack) with a reverse temperature distribution. Furthermore, this “45-20” pack shows similar trends to the pack with isothermal conditions of 32.5 °C. This is because cells closest to the load point already experience lower currents compared to cells further away due to the influence of the uneven resistances. Under the “45-20” configuration this further amplifies the uneven current balancing since it reduces the internal resistance of the cell already providing more current, thus leading to reduced pack performance.

In order to diagnose such problems, the ICA plots of the battery pack with different temperature distributions is presented in Fig. 10(b). The peak of battery pack (“45-all”) is the highest because of its high accessible capacity, while the pack with isothermal low temperature 20 °C is the lowest. Furthermore, the peak positions shift to higher potentials with higher temperatures due to the decreased cell polarisation resistance. ICA as a method for diagnosing single cells is well acknowledged in the academic literature however works focusing on the ICA profiles of packs we more seldom found. An exception is the work by

Weng et al. [57] who highlighted its applicability in battery packs and in its ability to monitor the state-of-health. Here, however, we highlight the importance of considering the thermal conditions which the ICA profiles are extracted under, with the influence of thermal gradients causing significant changes in the spectra.

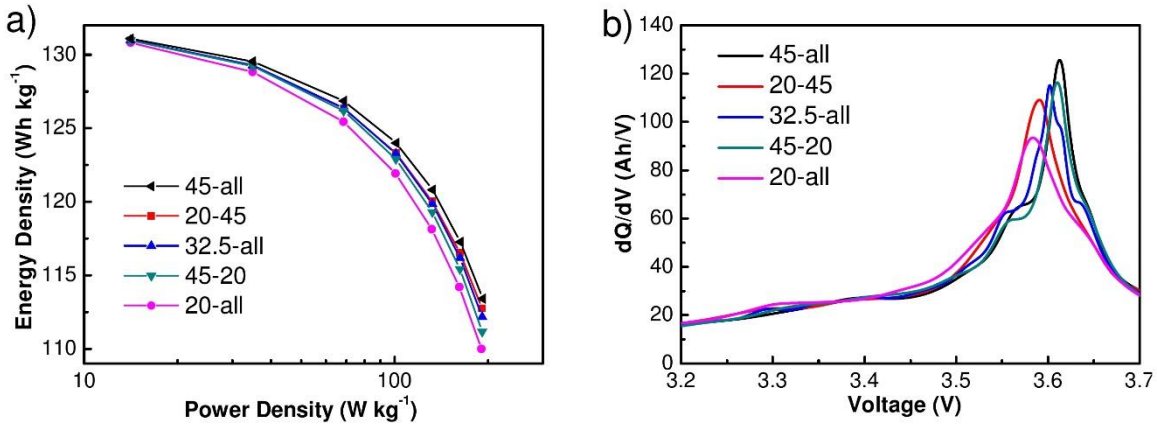

Fig. 10. a) Simulated ragone plot for battery packs with different temperature distributions. b) Simulated incremental capacity analysis plots for different thermal conditions for battery packs under 1 C constant current discharge.

These uneven thermal conditions clearly affect the energy and power density of the modelled battery packs, with higher temperatures enabling better performance, however the lifetime implications also need to be considered. Simulated battery packs with different thermal gradients were cycled at 1C between the 4.2-2.7 V window. The output energy of cells during the charge/discharge cycles is given in Fig. 11. Considering the connection resistance between cells, the cell closer to the load point provides the highest output energy, and this difference is enlarged if the “45-20” temperature distribution is applied as in Fig. 11(a). The difference in output energy for all six cells is the smallest in Fig. 11(b) where the “20-45” thermal condition is applied. Furthermore, in all cases it can be seen that cells all degrade at different rates within the battery pack, with the variation being the highest when a thermal gradient is applied. In the isothermal condition, differences in the cell-to-cell degradation rate is due to the different durations that the cell spends at different SOCs, since the SEI layer growth kinetics is related to the anode potential.

An overview of the energy output and lifetime of the battery packs under different thermal conditions is shown in Fig. 11(d). The 2nd cycle pack energy output is presented as the first cycle is higher than the 2nd cycle due to the 1st cycle being at steady state and thus not in dynamic equilibrium. When applying the lower temperature to B1 and higher temperature away from the load point, the “20-45” pack provides a similar output energy to the isothermal counterpart (“32.5-all” pack), which is 1.14% higher than the “45-20” pack with a reverse temperature gradient. In terms of degradation rate, there is a deviation of 5.2%, from -7.71 mWh/cycle (isothermal 32.5 °C) to -8.11 mWh/cycle, in non-isothermal conditions for the “20-45” pack. Similar trends can be found in the results for battery pack output capacity in Fig. S4.

The rationale for this difference in performance under different thermal conditions is related to coupled behavior between temperature, resistance and current distribution in parallel strings. Under the isothermal “32.5-all” condition, cells provide heterogeneous currents due to the interconnection resistances. When the “45-20” temperature gradient is applied, this

increases the level of current heterogeneity since this increases the resistance of the lowest performing cell (B6) relative to the best one (B1). This localized stressing of a particular cell decreases the accessible energy and also accelerates the pack degradation. In the case of the “20-45” thermal gradient this helps to homogenize the currents by decreasing the resistance of the worst performing cell relative to the best one. Thus, the direction of the thermal gradient in a battery pack is important as this can affect the uneven current distributions. In the case considered here, the “20-45” pack configuration had a comparable energy output to the “32.5-all” pack but with a higher degradation rate. This thus highlights the need to maintain even thermal conditions for maximization of lifetime, as shown in Fig. 12.

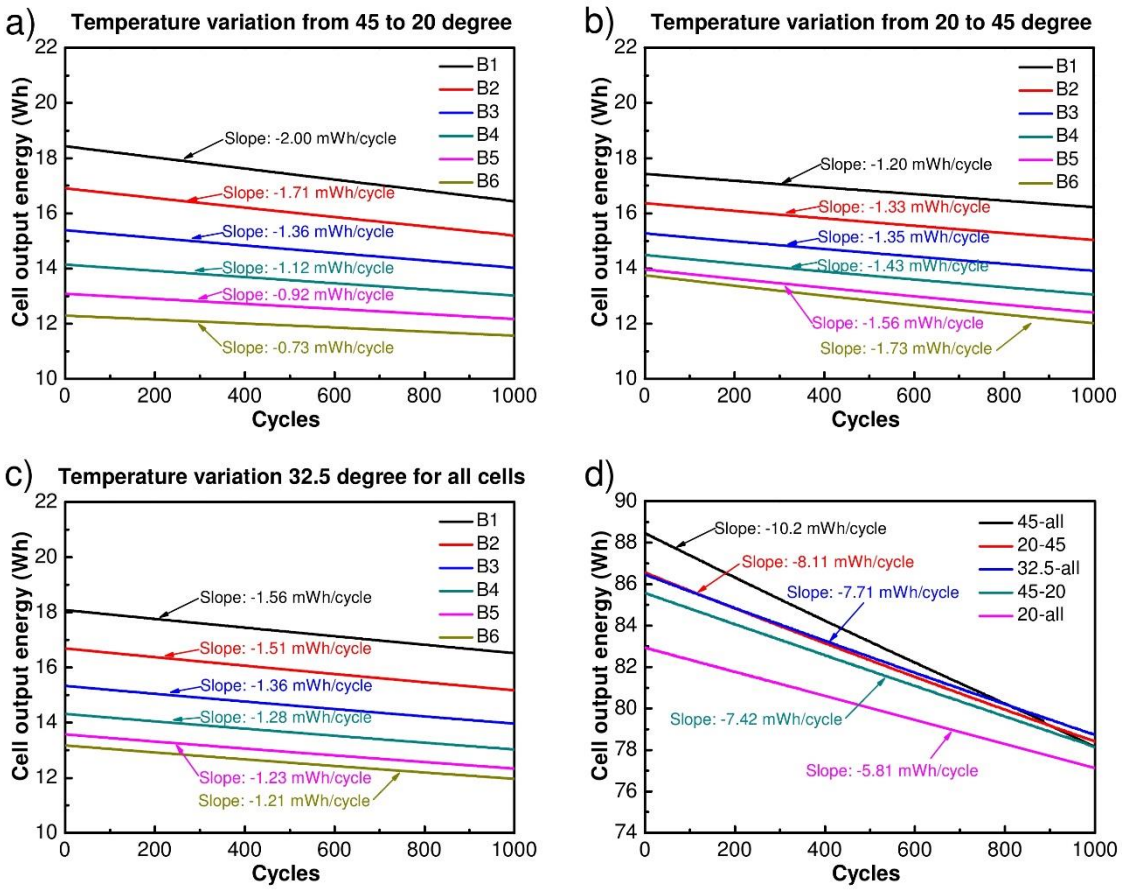

Fig. 11. Simulated discharge energy loss for battery packs with thermal gradients under 1 C constant current cycling: a) 45 to 20 °C decreasing by 5 °C for cells B1 to B6; b) 20 to 45 °C increasing by 5 °C for cells B1 to B6; c) 32.5 °C for all cells; d) pack output energy during cycling and degradation rates.

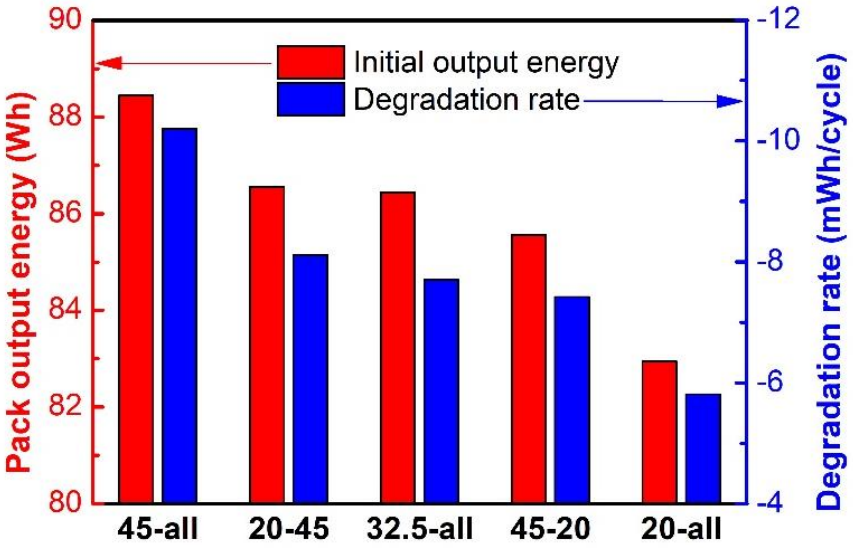

Fig. 12. The simulation results of effect of temperature gradients on the pack output energy for the second cycle and degradation rates.

It should be noted that the simulated degradation rates shown in Fig. 12 currently only account for the growth of the SEI layer. In reality other degradation modes such as particle fracture, cathode dissolution and electrolyte decomposition can also affect the lifetime performance of a cell/pack. This is the subject of future modelling and experimental work.

Conclusions

A thermally coupled SPM which includes a SEI layer growth degradation mechanism is used to investigate the impact of cell-to-cell variations, interconnection resistances and thermal gradients on battery pack performance and lifetime. The model highlights the fact that interconnect resistances in parallel battery strings can cause uneven current distributions, with the highest load being experienced near the load points, with the standard deviation between cell currents increasing with higher loads. Simulations show good agreement with experimental data for C-rates up to 0.5 C, however the simulations show a slight underestimation of current at higher C-rates due to the absence of concentration gradients in the SPM; underestimating the polarisation losses.

In the case where a cell with a higher impedance is added to the parallel string, the placement of the cell can affect the output energy. If a higher impedance cell is placed closest to the load point, this has the beneficial impact of equalising current distributions, however if placed in a location further from the load point this exasperates the problem, leading to reduced performance. From the simulations performed, a difference of 6% in energy output was observed for different configurations at a discharge rate of 1.5 C.

Simulation of different thermal gradients, show also that the current heterogeneity can be further influenced by the cell temperature. As temperature uniformly increases, there is a clear increase in the accessible energy and power due to the increased chemical kinetics and solid-state diffusion properties of the electrodes. Unfortunately, this also leads to an increase in the degradation rate. In the case where thermal gradients are applied, the direction of this relative to the cells affects the pack performance. In the case where higher

temperatures are applied to cells providing less current due to interconnect resistances, the thermal gradient helped to decrease the standard deviation of currents between cells. In the simulations run, it was shown that a thermal gradient of “20-45” exhibited nearly the same output capacity as the uniform “32.5-all” pack, however the degradation rate was 5.2% higher.

Nonetheless, although the current simulation in this paper only considers the SEI layer growth, the proposed modelling framework can still be used to further evaluate the performance and lifetime of different battery pack configurations under varying operating conditions. In the future, other degradation modes which can also affect the lifetime performance of a cell/pack, such as mechanical fracture of the electrodes, will be considered in future modelling and experimental work.

Acknowledgements

The authors would like to thank Dr. Chris Dent and Dr. Fanlin Meng for their discussions around the work. This work was kindly supported by the EPSRC energy storage for low carbon grids project (EP/K002252/1), the EPSRC Joint UK-India Clean Energy centre (JUICE)(EP/P003605/1), the EPSRC Faraday Institution Multi-Scale Modelling project (EP/S003053/1, grant number FIRG003) and the Innovate UK Advanced Battery Lifetime Extension (ABLE) project.

References

[1] S. Zhang, R. Xiong, Adaptive energy management of a plug-in hybrid electric vehicle based on driving pattern recognition and dynamic programming, Appl. Energy. 155 (2015) 68–78. doi:10.1016/j.apenergy.2015.06.003.

[2] D. Ren, X. Liu, X. Feng, L. Lu, M. Ouyang, J. Li, X. He, Model-based thermal runaway prediction of lithium-ion batteries from kinetics analysis of cell components, Appl. Energy. 228 (2018) 633–644. doi:10.1016/j.apenergy.2018.06.126.

[3] R. Xiong, Y. Duan, J. Cao, Q. Yu, Battery and ultracapacitor in-the-loop approach to validate a real-time power management method for an all-climate electric vehicle, Appl. Energy. 217 (2018) 153–165. doi:10.1016/j.apenergy.2018.02.128.

[4] R. Xiong, J. Cao, Q. Yu, Reinforcement learning-based real-time power management for hybrid energy storage system in the plug-in hybrid electric vehicle, Appl. Energy. 211 (2018) 538–548. doi:10.1016/j.apenergy.2017.11.072.

[5] X. Feng, C. Weng, M. Ouyang, J. Sun, Online internal short circuit detection for a large format lithium ion battery, Appl. Energy. 161 (2016) 168–180. doi:10.1016/j.apenergy.2015.10.019.

[6] F. Sun, R. Xiong, H. He, A systematic state-of-charge estimation framework for multi-cell battery pack in electric vehicles using bias correction technique, Appl. Energy. 162 (2016) 1399–1409. doi:10.1016/j.apenergy.2014.12.021.

[7] X. Feng, M. Ouyang, X. Liu, L. Lu, Y. Xia, X. He, Thermal runaway mechanism of lithium ion battery for electric vehicles: A review, Energy Storage Mater. 10 (2018) 246–267. doi:10.1016/j.ensm.2017.05.013.

[8] X. Feng, C. Xu, X. He, L. Wang, G. Zhang, M. Ouyang, Mechanisms for the evolution of cell variations within a LiNixCoyMnzO2/graphite lithium-ion battery pack caused by

temperature non-uniformity, J. Clean. Prod. 205 (2018) 447–462. doi:10.1016/j.jclepro.2018.09.003.

[9] X. Feng, X. He, M. Ouyang, L. Lu, P. Wu, C. Kulp, S. Prasser, Thermal runaway propagation model for designing a safer battery pack with 25Ah LiNixCoyMnzO2 large format lithium ion battery, Appl. Energy. 154 (2015) 74–91. doi:10.1016/j.apenergy.2015.04.118.

[10] K. Rumpf, M. Naumann, A. Jossen, Experimental investigation of parametric cell-to-cell variation and correlation based on 1100 commercial lithium-ion cells, J. Energy Storage. 14 (2017) 224–243. doi:10.1016/J.EST.2017.09.010.

[11] T. Baumhöfer, M. Brühl, S. Rothgang, D.U. Sauer, Production caused variation in capacity aging trend and correlation to initial cell performance, J. Power Sources. 247 (2014) 332–338. doi:10.1016/j.jpowsour.2013.08.108.

[12] S.J. Harris, D.J. Harris, C. Li, Failure statistics for commercial lithium ion batteries: A study of 24 pouch cells, J. Power Sources. 342 (2017) 589–597. doi:10.1016/J.JPOWSOUR.2016.12.083.

[13] B. Wu, V. Yufit, M. Marinescu, G.J. Offer, R.F. Martinez-Botas, N.P. Brandon, Coupled thermal-electrochemical modelling of uneven heat generation in lithium-ion battery packs, J. Power Sources. 243 (2013) 544–554. doi:10.1016/j.jpowsour.2013.05.164.

[14] M.J. Brand, M.H. Hofmann, M. Steinhardt, S.F. Schuster, A. Jossen, Current distribution within parallel-connected battery cells, J. Power Sources. 334 (2016) 202–212. doi:10.1016/J.JPOWSOUR.2016.10.010.

[15] M. Dubarry, A. Devie, B.Y. Liaw, Cell-balancing currents in parallel strings of a battery system, J. Power Sources. 321 (2016) 36–46. doi:10.1016/J.JPOWSOUR.2016.04.125.

[16] J. Kim, B.H. Cho, Screening process-based modeling of the multi-cell battery string in series and parallel connections for high accuracy state-of-charge estimation, Energy. 57 (2013) 581–599. doi:10.1016/J.ENERGY.2013.04.050.

[17] L. Zhong, C. Zhang, Y. He, Z. Chen, A method for the estimation of the battery pack state of charge based on in-pack cells uniformity analysis, Appl. Energy. 113 (2014) 558–564. doi:10.1016/J.APENERGY.2013.08.008.

[18] W. Shi, X. Hu, C. Jin, J. Jiang, Y. Zhang, T. Yip, Effects of imbalanced currents on large-format LiFePO4/graphite batteries systems connected in parallel, J. Power Sources. 313 (2016) 198–204. doi:10.1016/J.JPOWSOUR.2016.02.087.

[19] T.R. Ashwin, A. McGordon, P.A. Jennings, Electrochemical modelling of Li-ion battery pack with constant voltage cycling, J. Power Sources. 341 (2017) 327–339. doi:10.1016/J.JPOWSOUR.2016.11.092.

[20] A LiFePO4 battery pack capacity estimation approach considering in-parallel cell safety in electric vehicles, Appl. Energy. 142 (2015) 293–302. doi:10.1016/J.APENERGY.2014.12.081.

[21] K.-C. Chiu, C.-H. Lin, S.-F. Yeh, Y.-H. Lin, C.-S. Huang, K.-C. Chen, Cycle life analysis of series connected lithium-ion batteries with temperature difference, J. Power Sources. 263 (2014) 75–84. doi:10.1016/J.JPOWSOUR.2014.04.034.

[22] L. Zhou, Y. Zheng, M. Ouyang, L. Lu, A study on parameter variation effects on

battery packs for electric vehicles, J. Power Sources. 364 (2017) 242–252. doi:10.1016/J.JPOWSOUR.2017.08.033.

[23] C. Zhang, Y. Jiang, J. Jiang, G. Cheng, W. Diao, W. Zhang, Study on battery pack consistency evolutions and equilibrium diagnosis for serial- connected lithium-ion batteries, Appl. Energy. 207 (2017) 510–519. doi:10.1016/J.APENERGY.2017.05.176.

[24] N. Ganesan, S. Basu, K.S. Hariharan, S.M. Kolake, T. Song, T. Yeo, D.K. Sohn, S. Doo, Physics based modeling of a series parallel battery pack for asymmetry analysis, predictive control and life extension, J. Power Sources. 322 (2016) 57–67. doi:10.1016/J.JPOWSOUR.2016.05.005.

[25] G.J. Offer, V. Yufit, D.A. Howey, B. Wu, N.P. Brandon, Module design and fault diagnosis in electric vehicle batteries, J. Power Sources. 206 (2012) 383–392. doi:10.1016/j.jpowsour.2012.01.087.

[26] R. Carter, B. Huhman, C.T. Love, I. V. Zenyuk, X-ray computed tomography comparison of individual and parallel assembled commercial lithium iron phosphate batteries at end of life after high rate cycling, J. Power Sources. 381 (2018) 46–55. doi:10.1016/J.JPOWSOUR.2018.01.087.

[27] F. An, J. Huang, C. Wang, Z. Li, J. Zhang, S. Wang, P. Li, Cell sorting for parallel lithium-ion battery systems: Evaluation based on an electric circuit model, J. Energy Storage. 6 (2016) 195–203. doi:10.1016/J.EST.2016.04.007.

[28] L. Wang, Y. Cheng, X. Zhao, Influence of connecting plate resistance upon LiFePO4 battery performance, Appl. Energy. 147 (2015) 353–360. doi:10.1016/J.APENERGY.2015.03.016.

[29] Y. Zheng, M. Ouyang, L. Lu, J. Li, X. Han, L. Xu, H. Ma, T.A. Dollmeyer, V. Freyermuth, Cell state-of-charge inconsistency estimation for LiFePO4 battery pack in hybrid electric vehicles using mean-difference model, Appl. Energy. 111 (2013) 571–580. doi:10.1016/J.APENERGY.2013.05.048.

[30] R. Gogoana, M.B. Pinson, M.Z. Bazant, S.E. Sarma, Internal resistance matching for parallel-connected lithium-ion cells and impacts on battery pack cycle life, J. Power Sources. 252 (2014) 8–13. doi:10.1016/J.JPOWSOUR.2013.11.101.

[31] Y. Merla, B. Wu, V. Yufit, N.P. Brandon, R.F. Martinez-Botas, G.J. Offer, Extending battery life: A low-cost practical diagnostic technique for lithium-ion batteries, J. Power Sources. 331 (2016) 224–231. doi:10.1016/j.jpowsour.2016.09.008.

[32] Y. Merla, B. Wu, V. Yufit, R.F. Martinez-Botas, G.J. Offer, An easy-to-parameterise physics-informed battery model and its application towards lithium-ion battery cell design, diagnosis, and degradation, J. Power Sources. 384 (2018). doi:10.1016/j.jpowsour.2018.02.065.

[33] Y. Merla, B. Wu, V. Yufit, N.P. Brandon, R.F. Martinez-Botas, G.J. Offer, Novel application of differential thermal voltammetry as an in-depth state-of-health diagnosis method for lithium-ion batteries, J. Power Sources. 307 (2016) 308–319. doi:10.1016/j.jpowsour.2015.12.122.

[34] B. Wu, V. Yufit, Y. Merla, R.F. Martinez-Botas, N.P. Brandon, G.J. Offer, Differential thermal voltammetry for tracking of degradation in lithium-ion batteries, J. Power Sources. 273 (2015) 495–501. doi:10.1016/j.jpowsour.2014.09.127.

[35] N. Yang, X. Zhang, B. Shang, G. Li, Unbalanced discharging and aging due to temperature differences among the cells in a lithium-ion battery pack with parallel combination, J. Power Sources. 306 (2016) 733–741. doi:10.1016/J.JPOWSOUR.2015.12.079.

[36] T. Bruen, J. Marco, Modelling and experimental evaluation of parallel connected lithium ion cells for an electric vehicle battery system, J. Power Sources. 310 (2016) 91–101. doi:10.1016/J.JPOWSOUR.2016.01.001.

[37] S. Miyatake, Y. Susuki, T. Hikihara, S. Itoh, K. Tanaka, Discharge characteristics of multicell lithium-ion battery with nonuniform cells, J. Power Sources. 241 (2013) 736–743. doi:10.1016/j.jpowsour.2013.05.179.

[38] S. Nejad, D.T. Gladwin, D.A. Stone, A systematic review of lumped-parameter equivalent circuit models for real-time estimation of lithium-ion battery states, J. Power Sources. 316 (2016) 183–196. doi:10.1016/J.JPOWSOUR.2016.03.042.

[39] K.S. Hariharan, V. Senthil Kumar, A nonlinear equivalent circuit model for lithium ion cells, J. Power Sources. 222 (2013) 210–217. doi:10.1016/j.jpowsour.2012.08.090.

[40] H.-T. Lin, T.-J. Liang, S.-M. Chen, Estimation of Battery State of Health Using Probabilistic Neural Network, IEEE Trans. Ind. Informatics. 9 (2013) 679–685. doi:10.1109/TII.2012.2222650.

[41] X. Hu, S.E. Li, Y. Yang, Advanced Machine Learning Approach for Lithium-Ion Battery State Estimation in Electric Vehicles, IEEE Trans. Transp. Electrif. 2 (2016) 140–149. doi:10.1109/TTE.2015.2512237.

[42] M. Guo, G.-H. Kim, R.E. White, A three-dimensional multi-physics model for a Li-ion battery, J. Power Sources. 240 (2013) 80–94. doi:10.1016/j.jpowsour.2013.03.170.

[43] K. Smith, C.-Y. Wang, Power and thermal characterization of a lithium-ion battery pack for hybrid-electric vehicles, J. Power Sources. 160 (2006) 662–673. doi:10.1016/j.jpowsour.2006.01.038.

[44] L. Cai, R.E. White, Mathematical modeling of a lithium ion battery with thermal effects in COMSOL Inc. Multiphysics (MP) software, J. Power Sources. 196 (2011) 5985–5989. doi:10.1016/J.JPOWSOUR.2011.03.017.

[45] S. Santhanagopalan, Q. Guo, P. Ramadass, R.E. White, Review of models for predicting the cycling performance of lithium ion batteries, J. Power Sources. 156 (2006) 620–628. doi:10.1016/j.jpowsour.2005.05.070.

[46] J. Newman, K.E. Thomas, H. Hafezi, D.R. Wheeler, Modeling of lithium-ion batteries, J. Power Sources. 119 (2003) 838–843. doi:10.1016/S0378-7753(03)00282-9.

[47] M. Doyle, J. Newman, Comparison of Modeling Predictions with Experimental Data from Plastic Lithium Ion Cells, J. Electrochem. Soc. 143 (1996) 1890. doi:10.1149/1.1836921.

[48] J. Christensen, J. Newman, A Mathematical Model for the Lithium-Ion Negative Electrode Solid Electrolyte Interphase, J. Electrochem. Soc. 151 (2004) A1977. doi:10.1149/1.1804812.

[49] C. Patsios, B. Wu, E. Chatzinikolaou, D.J. Rogers, N. Wade, N.P. Brandon, P. Taylor, An integrated approach for the analysis and control of grid connected energy storage systems, J. Energy Storage. 5 (2016) 48–61. doi:10.1016/j.est.2015.11.011.

[50] M. Guo, G. Sikha, R.E. White, Single-Particle Model for a Lithium-Ion Cell: Thermal Behavior, J. Electrochem. Soc. 158 (2011) A122. doi:10.1149/1.3521314.

[51] S. Santhanagopalan, R.E. White, Online estimation of the state of charge of a lithium ion cell, J. Power Sources. 161 (2006) 1346–1355. doi:10.1016/j.jpowsour.2006.04.146.

[52] N. Chaturvedi, R. Klein, Algorithms for advanced battery-management systems, Control Syst. …. (2010) 49–68. doi:10.1109/MCS.2010.936293.

[53] P. Ramadass, B. Haran, P.M. Gomadam, R. White, B.N. Popov, Development of First Principles Capacity Fade Model for Li-Ion Cells, J. Electrochem. Soc. 151 (2004) A196. doi:10.1149/1.1634273.

[54] Y. Troxler, B. Wu, M. Marinescu, V. Yufit, Y. Patel, A.J. Marquis, N.P. Brandon, G.J. Offer, The effect of thermal gradients on the performance of lithium-ion batteries, J. Power Sources. (2013) 1–8. doi:10.1016/j.jpowsour.2013.06.084.

[55] P. Taheri, S. Hsieh, M. Bahrami, Investigating electrical contact resistance losses in lithium-ion battery assemblies for hybrid and electric vehicles, J. Power Sources. 196 (2011) 6525–6533. doi:10.1016/j.jpowsour.2011.03.056.

[56] M.I. Ardani, Y. Patel, A. Siddiq, G.J. Offer, R.F. Martinez-Botas, Combined experimental and numerical evaluation of the differences between convective and conductive thermal control on the performance of a lithium ion cell, Energy. 144 (2018) 81–97. doi:10.1016/j.energy.2017.12.032.

[57] C. Weng, X. Feng, J. Sun, H. Peng, State-of-health monitoring of lithium-ion battery modules and packs via incremental capacity peak tracking, Appl. Energy. 180 (2016) 360–368. doi:10.1016/j.apenergy.2016.07.126.